A mechanical TiAl/TiAlN multinanolayer coating model based on microstructural analysis and nanoindentation

S. Giljean[a], Y. Gaillard[b], C. Rousselot[c], C. Bouillet[d], M. Lenertz[e]
F. Richard[b], M-J. Pac[a]

[a] Université de Haute-Alsace, LPMT UR 4365, 68093 Mulhouse, France
marie-jose.pac@uha.fr
sylvain.giljean@uha.fr
[b] Université de Franche-Comté, CNRS, institut FEMTO-ST UMR 6174, F-25000 Besançon, France
fabrice.richard@univ-fcomte.fr
yves.gaillard@univ-fcomte.fr
[c] Université de Franche-Comté, CNRS, institut FEMTO-ST UMR 6174, F-25200 Montbéliard, France
christophe.rousselot@univ-fcomte.fr
[d] Plateforme MACLE-CVL, UAR2590, 45071 Orléans Cedex 2 - France
corinne.bouillet@cnrs-orleans.fr
[e] Institut de Physique et Chimie des Matériaux de Strasbourg - CNRS UMR 7504, 67034 Strasbourg, France
marc.lenertz@ipcms.unistra.fr

Keywords: multilayer TiAl/TiAlN – based coatings, structural properties, electron energy loss spectroscopy, nanoindentation, inverse method, FEMU

Graphical Abstract

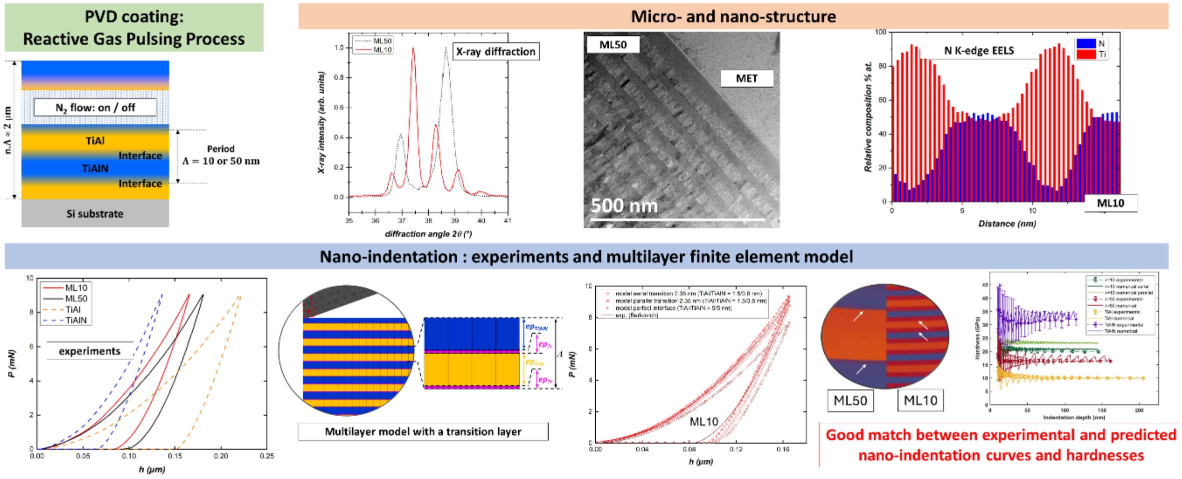

Abstract

A finite element model reproducing the mechanical behaviour during nanoindentation tests on $Ti_{0.67}Al_{0.33}$ / $Ti_{0.54}Al_{0.46}N$ multilayer coatings was developed. Coatings with two different nanoperiods (10 and 50 nm) were deposited by radio-frequency magnetron sputtering from a single sintered titanium/aluminium target using the reactive gas pulsing process. X-ray diffraction and transmission electron microscopy confirmed the multilayer stacking of the coatings. The finite element models of coatings with these two stacking periods were built considering successive hypotheses: equal thicknesses for metal and nitride nanolayers stacked without transition layer, equal thicknesses stacking with a transition layer between each metal and nitride nanolayer and finally imbalanced thicknesses stacking with a transition layer. The elastic and plastic properties of the stacked nanolayers were determined on thick monolithic coatings of metal and nitride using indentation testing and the finite element model updating method respectively. The elastic-plastic properties of the interface were introduced in the multilayer model as a rule of mixtures of the metal and nitride properties using two hypotheses: parallel or serial. For 50 nm-period film, the interface has a negligible effect on the overall indentation response. On the other hand, for the 10 nm period, the imbalanced stacking model with precise knowledge of the transition layer thickness obtained by N K-edge electron energy loss spectroscopy is required to reproduce the experimental indentation curve. Compared to classical analytical models accounting for hardness, not only the hardnesses but also the indentation moduli appear to be well predicted and evaluated in this work.

1 Introduction

Very hard thin coatings are now commonly used to protect cutting tools in metalworking industries, to lengthen tool life and increase cutting performance. Metal nitrides like TiN, (Ti,Al)N and metal carbides such as TiC, WC are commonly used [1–3]. However, hard coatings, as hard bulk materials, have a serious drawback, namely their poor fracture toughness [4,5]. Structured as a multilayered coating by alternating a soft and a hard layer, it is possible to improve the fracture toughness of the coating while maintaining a hardness suitable for the targeted applications, since the good performance of the coating results from the synergy of the properties of each of the constituent layers [6–9]. In such coatings, the thickness of the hard layer becomes nanometric and very similar to a high shape ratio object more conducive to fracture resistance. For these structured materials, the mechanical strength of the interfaces plays a key role [10–14]. Weak interfaces allow mechanical energy to dissipate and may initiate crack bifurcation and indeed may, under certain conditions, interrupt the inexorable rupture of the film [15,16]. A strong interface allows continuity of the deformation from one layer to another. In the case of an alternation of hard/soft layers, the multilayered structures become more resilient and can reach very high deformation states without breaking.

Having a finite element model (FEM) of the multilayer able to reproduce its mechanical response [17,18] is an essential prerequisite to the optimised design of metal/nitride multilayer coatings [19–21]. The properties of $Ti_{1-x}Al_xN$ films are highly dependent on Al content and deposition process as well as the change of crystallographic structure [22–25]. In $Ti_{1-x}Al_xN$ ternary nitrides, mechanical performances are improved when Al is substituted for a part of the Ti atoms in an fcc lattice, and it has been conclusively demonstrated that coatings whose x Al content is around 50 at.%. exhibit the best mechanical properties when magnetron sputtering is used [26]. This deposition technique leads to ordered materials having a defined composition and growing as columnar domains made of oriented nanocrystallites with cubic or hexagonal symmetry depending on Al content [27]. The main objective of this work is the mechanical modelling of the $Ti_{0.67}Al_{0.33}/Ti_{0.54}Al_{0.46}N$ multilayer coatings.

Experimental identification of the material's behaviour of the different compounds in the multilayer, namely the $Ti_{0.67}Al_{0.33}$ metal (labelled TiAl) and $Ti_{0.54}Al_{0.46}N$ nitride (labelled TiAlN) elements, is necessary to the development of a numerical model reproducing the mechanical response of the multilayer coating. Instrumented indentation has been chosen for this work because this experimental probe offers the particular advantage of allowing the characterisation of thin film materials. However, accessing the parameters of the material by indentation is not a trivial matter, especially for the plastic properties. It is well known that, in numerical terms, different material behaviours can lead to the same indentation load-displacement response [28]. To overcome this critical issue, the experiment design is guided by an identifiability index, already presented elsewhere [29,30], which ensures the encountered solution is reliable. This identifiability analysis leads to the use of two different indenter tip shapes (Berkovich and cube corner) to ensure uniqueness of the solution. The identification of the plastic parameters of TiAl and TiAlN monolithic layers is then performed using the Finite Element Model Updating (FEMU) method, which consists of minimising the gap between experimental and numerical indentation curves.

In the particular case where two layers are linked at crystallographic level, the interface constitutes a third compound. For example, in the case of Cr/CrN coatings, a Cr_2N transition layer is formed between the Cr and CrN layers [31]. Depending on the thickness and the number of each layer, the volume ratio of this third compound can reach a nonnegligible portion. In this way, a multilayer material apparently composed of two materials, A and B, is actually a three-layer material. It is then possible to understand why for some particular multilayers, the mechanical properties of the coating are outside the limit set by the properties specific to the two compounds [32–36]. In these cases, mechanical characterisation is even more complicated as three materials have to be identified. The complexity of the multilayer FEM implemented in this study could only be optimised by conducting a fine analysis of the micro and nanostructure of the films, especially in the thickness. So, in addition to conventional XRD characterisation, transmission electron microscopy and spectroscopy were used for these characterisations. Plastic behaviours were identified for both TiAl and TiAlN monolithic layers and validated using TiAl/TiAlN multilayer coating applied using a shutter in front of the target between the sputtering process for each metal and nitride layer and a FEM of the coating assuming stacking without transition layer. These calculations show that models without a transition layer between TiAl and TiAlN allow good reproduction of the indentation response of multilayers with high stack period values. However, they do not match at all for small period values. The influence of a transition layer between TiAl and TiAlN becomes preponderant as the period decreases. The end of the paper is then dedicated to the identification of the behaviour of this transition layer and the interpretation of the link between the hypotheses concerning the interface behaviour and the actual nanostructure.

2 Materials and Methods

2.1 Mono- and multilayer coating preparation

Thin $Ti_{0.67}Al_{0.33}$, $Ti_{0.54}Al_{0.46}N$ monolithic and $Ti_{0.67}Al_{0.33}/Ti_{0.54}Al_{0.46}N$ multilayer coatings, were deposited onto (100) silicon substrates, in an Alliance Concept AC450 vacuum reactor, by radio-frequency magnetron sputtering from a sintered titanium/aluminium 66/33 at.% metallic target (purity 99.99% and diameter 50 mm) at room temperature, in an Ar or Ar+N_2 atmosphere. All the depositions were carried out with an argon partial pressure of 0.52 Pa. More details on the deposition parameters (gas pressure, bias, target-substrate distance, etc.) and diffraction pattern of the target are presented in [20,37]. A 45 nm $Ti_{0.67}Al_{0.33}$ buffer layer was systematically deposited on the etched substrates to enhance film adhesion.

First two monolithic films, metallic $Ti_{0.67}Al_{0.33}$ and titanium aluminium nitride $Ti_{0.54}Al_{0.46}N$ were prepared using a constant nitrogen flow rate of 0 and 1 sccm, respectively. The maximum N_2 flow rate was high enough to sputter the target in the nitride mode to obtain nitrogen stoichiometry coatings.

Secondly, multilayered films with two different periods were deposited using the reactive gas pulsing process (RGPP) [38] to nanostratify the coating by alternating $Ti_{0.67}Al_{0.33}$ and $Ti_{0.54}Al_{0.46}N$ layers. The nitrogen flow rate was periodically pulsed using a quasi-rectangular wave function between a minimum and a maximum rate of 0 and 1 sccm respectively. Based on the deposition rate of the $Ti_{0.67}Al_{0.33}$ and $Ti_{0.54}Al_{0.46}N$ single-layered films, the pulse periods 90 s and 480 s were chosen to obtain stacking periods Λ = 10 and 50 nm respectively. For easier reading of the paper, $Ti_{0.67}Al_{0.33}$ and $Ti_{0.54}Al_{0.46}N$ are respectively written as TiAl and TiAlN and the deposited samples are summarised in Table 1. The expected period Λ is defined by $\Lambda = \lambda_{TiAl} + \lambda_{TiAlN}$, where λ_{TiAl}, λ_{TiAlN} are the same expected thicknesses for TiAl alloy and TiAlN nitride respectively. All the as-deposited multilayer coatings have a TiAlN upper layer. A last sample was deposited with a 50 nm period using a shutter in front of the target introduced between each deposit of TiAl and TiAlN to minimise nitrogen contamination of the interfaces when the N_2 flow rate was 0 sccm and thus to have sharper interfaces, without a transition layer between the metal/nitride layers. This sample allowed the validation of the plastic parameters of each monolithic layer identified using the FEMU method as described in section 3.2.

Sample name	Sample type	Period Λ (nm)	thickness ep (nm)
TiAl	$Ti_{0.67}Al_{0.33}$	/	2500
TiAlN	$Ti_{0.54}Al_{0.46}N$	/	2950
ML10	$(Ti_{0.67}Al_{0.33}/Ti_{0.54}Al_{0.46}N)_n$	10	1790
ML50	$(Ti_{0.67}Al_{0.33}/Ti_{0.54}Al_{0.46}N)_n$	50	2000
ML50s	$(Ti_{0.67}Al_{0.33}/Ti_{0.54}Al_{0.46}N)_n$	50 with shutter	1970

Table 1: Characteristics of the monolithic and multilayer coatings. The film thicknesses were measured by the step method using a mechanical profilometer.

2.2 Micro- and nanostructural characterisations

To investigate the structure of the coatings, X-Ray Diffraction (XRD) and Transmission Electron Microscopy (TEM) were used. The XRD experiments were carried out using a Rigaku Smartlab X-ray diffractometer, equipped with a 9kW Cu source ($\lambda_{K\alpha 1}$ = 1.54056 Å) and a Ge (220) two-bounce front monochromator. XRD patterns were recorded at room temperature in parallel-beam geometry.

TEM was used on the cross-section of the coatings to get deeper insights into the microstructure of the stacking. Cross-sections were prepared by focused ion beam milling and were then analysed using a Cs-corrected JEOL 2100F microscope, operating at 200 kV and equipped with an Electron Energy Loss Spectrometer (EELS), a Gatan Imaging Filter (GIF) spectrometer and a JEOL Energy Dispersive Spectrometer (EDS). The morphology and crystalline structure were studied by Selected Area Electron Diffraction (SAED). The chemistry of the nanolayers was determined by EELS and EDS profile along the growth direction, at different depths from the surface on a cross-section, by Scanning Transmission Electron Microscopy (STEM) using a 0.15 nm probe. N K-edge electron energy loss near edge structure (ELNES) spectra of the films were recorded with the GIF spectrometer using a dispersion of 0.2 eV energy per channel in order to record the Ti L edge too. The Al/Ti ratio was determined by EDS profile.

2.3 Plastic properties of the monolithic layers from nanoindentation

2.3.1 Nanoindentation experiments

Nanoindentation tests were performed using an Anton Paar UNHT (Ultra Nano-Indentation Hardness Tester). The indentation modulus of the films was calculated from the unloading path of indentation curves according to the Oliver and Pharr method [39,40]. Two indenter tip shapes were used (Berkovich and cube corner), mainly to ensure robustness of the inverse analysis method applied to extract the plastic parameters of the monolithic coatings, but also to provide validation data. The tip radii were 113 and 35 nm for the Berkovich and cube corner tips respectively.

2.3.2 Nanoindentation test model

The indentation test was modelled using a 2D axisymmetric FEM using the ANSYS software. Details of the finite element model can be found in [30]. The conical indenter was set with an equivalent half-angle α (70.30° for Berkovich and 42.28° for cube corner).

These angle values give the same contact area to depth ratio as a perfect Berkovich or cube corner tip. The tip blunting is modelled by an arc of circle of radius R. The coefficient of friction between the tip and the sample taken is $\mu = 0.1$ [41]. To minimise the effect of boundary conditions, the sample and tip sizes are 60 times greater than the maximum depth h_{max}. The area under the tip is finely meshed to a length of twice the thickness of the coating to accurately model the contact. In this area, the 4-node linear quadrilateral elements (PLANE 182) are initially square with an edge length equal to one-tenth of the maximum depth h_{max}. For the tip, quadratic triangular elements with 6 nodes (PLANE 183) are used. They have, at the level of the contact, a size equivalent to those of the sample. The mesh is gradually coarser away from the contact area, allowing computation time to be reduced. The nodes belonging to the lower surface of the modelled sample are embedded and a displacement is imposed on the upper surface of the indenter.

The diamond indenter tip (E_i = 1141 GPa, ν_i = 0.07) and Si substrate (E_s = 165 GPa, ν_s = 0.23) are considered as isotropic linear elastic materials. For the coatings an elastoplastic law with isotropic linear hardening is chosen.

The total strain tensor ε_{ij} can be separated into elastic and plastic components, respectively ε_{ij}^{e} and ε_{ij}^{p}, i.e.:

$$\varepsilon_{ij} = \varepsilon_{ij}^{e} + \varepsilon_{ij}^{p}. \tag{1}$$

The elastic component is driven by Young's modulus E and Poisson's ratio ν, the two intrinsic elastic parameters linking stress and elastic strain in Hooke's law, defined in the case of isotropic linear elastic materials by:

$$\sigma_{ij} = \frac{E}{1+\nu}\left(\varepsilon_{ij}^{e} + \frac{\nu}{1-2\nu}\varepsilon_{kk}^{e}\delta_{ij}\right). \tag{2}$$

σ_{ij} is the Cauchy stress tensor, ε_{kk}^{e} is the trace of the elastic strain tensor ε_{ij}^{e} and δ_{ij} is the Kronecker delta.

The plastic component is driven by the initial tensile yield stress σ_y and the isotropic hardening modulus H_p. They are related to the von Mises yield stress criterion, which defines the stress threshold from which the material plastically deforms.

In the case of a uniaxial tensile test, these assumptions on the elastic and plastic behaviour can be written as:

$$\sigma = E\varepsilon \qquad \text{for} \quad \sigma < \sigma_y \tag{3}$$

$$\sigma = \frac{EH_p}{E + H_p}\varepsilon \quad \text{for} \quad \sigma \geq \sigma_y. \tag{4}$$

where σ is the Cauchy tensile stress and ε is the logarithmic tensile strain.

For each layer, the behaviour is driven by two elastic parameters (E, ν) and two plastic parameters $\theta = (\theta_1, \theta_2) = (\sigma_Y, H_p)$. The Poisson's ratio values were taken from the literature and the Young's moduli were derived from indentation tests using the Continuous Stiffness Measurement (CSM) method. To identify the plastic parameters of the monolithic coatings ($\sigma_{Y,TiAl}$, $H_{p,TiAl}$, $\sigma_{Y,TiAlN}$, and $H_{p,TiAlN}$) from indentation curves, a method based on identifiability is used to design experiments to correctly pose the inverse problem, solved using Finite Element Model Updating (FEMU) method.

2.3.3 Finite element model updating (FEMU method)

The process of updating the numerical model based on the experimental data allows the estimation of 2 parameter values $\hat{\theta} = (\theta_1, \theta_2)$ which minimise the difference between the force $P(h;\theta)$ resulting from the finite element simulation and the experimental data $P^{exp}(h)$. The inverse problem is recast as the problem of minimising a cost function ω, which quantifies the difference between the numerical model and the experiment:

$$\hat{\theta} = \underset{\theta}{\operatorname{argmin}}\ \omega\ [P(h;\theta), P^{exp}(h)] \tag{5}$$

The cost function is minimised by a local numerical optimisation technique based on the LM algorithm [42,43] implemented by the MIC2M software [44]. A starting point is required in this algorithm. The influence of this point will therefore be investigated. The objective function is defined in displacement-controlled mode as [45]:

$$\omega(\theta) = \frac{1}{2}\sum_{e=1}^{n}\frac{1}{T^{(e)}}\left[\sum_{k=1}^{T^{(e)}}\left(\frac{P_k^{(e)}(\theta) - P_k^{exp^{(e)}}}{P_{max}^{(e)}}\right)^2\right] \tag{6}$$

$T^{(e)}$ is the number of data points for each nanoindentation test (e), i.e. number of simulated $P_k^{(e)}(\theta) = P_k^{(e)}\left(h_k^{(e)};\theta\right)$ and measured force $P_k^{exp^{(e)}} = P^{exp}(h_k^{(e)})$. $T^{(e)}$ is sufficiently large ($T^{(e)} > 100$) that it does not influence the reported results. $P_{max}^{(e)}$ is the maximum of the force (experimental for FEMU and a posteriori I-index, numerical for a priori I-index). In this paper $n = 1$ is a Berkovich test and $n = 2$ a cube corner test.

The uniqueness of the minimiser $\hat{\theta}$ is a fundamental question, particularly in instrumented nanoindentation. In fact, in the case of elastoplastic behaviour, numerous studies have shown that a group of materials with distinct elastoplastic properties may produce almost the same conical indentation $P\text{–}h$ curve [28,46,47]. It implies that the material properties cannot be uniquely determined by using a single sharp indenter tip. In order to address this problem in the case of elastoplastic behaviour, dual or multiple indentation techniques have been proposed by several authors [48–50]. However, the existence of mystical materials that give almost similar $P\text{–}h$ curves for different indenter tips has also been shown [51]. Recently, this problem of non-uniqueness of the elastoplastic properties was investigated by Phadikar et al. [52]. They found that non-uniqueness of the solution is caused by high sensitivity to the experimental errors. They also demonstrated that dual nanoindentation techniques are reliable when the experimental error is within $\pm 1\%$.

All these conclusions relate to bulk samples, perfect and rigid tip. In the case of TiAlN thin films with rounded and deformable tips, Pac et al. [19] shown that the identifiability is significantly improved. Whatever, the stability of the FEMU solution can be verified by performing an identifiability analysis.

2.3.4 Identifiability analysis to ensure reliable plastic properties.

Parameter identifiability analysis is used to quantify the reliability of the estimated parameters (a posteriori analysis) and to design the experiments that must be performed to obtain them in a robust way (a priori analysis). This approach is also known as *a priori* identifiability or structural identifiability, and depends only on the model and simulated data [53,54]. Indeed, a priori analysis can be done before the updating process and therefore does not require the experimental force $P^{exp}(t)$.

The identifiability analysis is first performed considering a single Berkovich nanoindentation test. Secondly, the combination of two tips is carried out: Berkovich and cube corner. The completeness of the data contained in the nanoindentation force is quantified by an I-index [29,30]. This index appears to be convenient to explore and investigate what the optimal experiments are which can extract the plastic parameters of a monolithic layer coating (initial yield stress and hardening modulus). The I-index is a measure of the conditioning of the inverse problem and is defined as:

$$I = \log_{10}\left(\frac{\lambda_{max}}{\lambda_{min}}\right) \tag{7}$$

where λ_{max} and λ_{min} are the maximum and minimum eigenvalues of a matrix $\bar{\mathbf{H}}$ at the considered calculation point $\theta = (\theta_1, \theta_2) = (\sigma_Y, H_p)$:

$$\bar{H}_{ij} = \theta_i \theta_j \sum_{e=1}^{n} \left[\frac{1}{\left(P_{max}^{(e)}\right)^2 T^{(e)}} \sum_{k=1}^{T} \frac{\partial P_k^{(e)}(\theta)}{\partial \theta_i} \frac{\partial P_k^{(e)}(\theta)}{\partial \theta_j} \right] \tag{8}$$

To calculate the numerical derivative in the previous equation with the forward finite difference method, each value parameter is changed by 0.5% with respect to its initial value.

The lower the I-index, the better the matrix is conditioned, which means its inverse can be calculated with great accuracy. On the other hand, if the I-index is large, the matrix is considered as ill-conditioned. This procedure allows the potentially identifiable combinations of material parameters ($I \leq 3$) to be distinguished, and good identifiability ($I < 2$) from those which are clearly not ($I > 3$). The evaluation of this index allows to overcome the $\pm 1\%$ experimental errors mentioned above [52]. In fact, too much sensitivity to experimental error will necessarily conduce to an index $I > 3$.

2.4 Some hypotheses for the multilayer model

2.4.1 Multilayer stacking without transition layer

The numerical model used for the multilayer coating is based on the FEM of the monolithic coating [30]. The coating is modelled as an assembly of TiAl and TiAlN nanolayers stacked alternately with a TiAl/TiAlN interface considered without thickness (Fig. 1a). The layer in contact with the indenter tip is a TiAlN layer and the layer above the substrate is a TiAl layer according to the deposition process. The thickness of each layer is defined as follows:

$$V_f \Lambda - e_{pTiAlN} = \left(1 - V_f\right)\Lambda - e_{pTiAl} = 0 \tag{9}$$

where V_f is the TiAlN volume fraction:

$$V_f = \frac{e_{pTiAlN}}{ep_{TiAl} + ep_{TiAlN}} \tag{10}$$

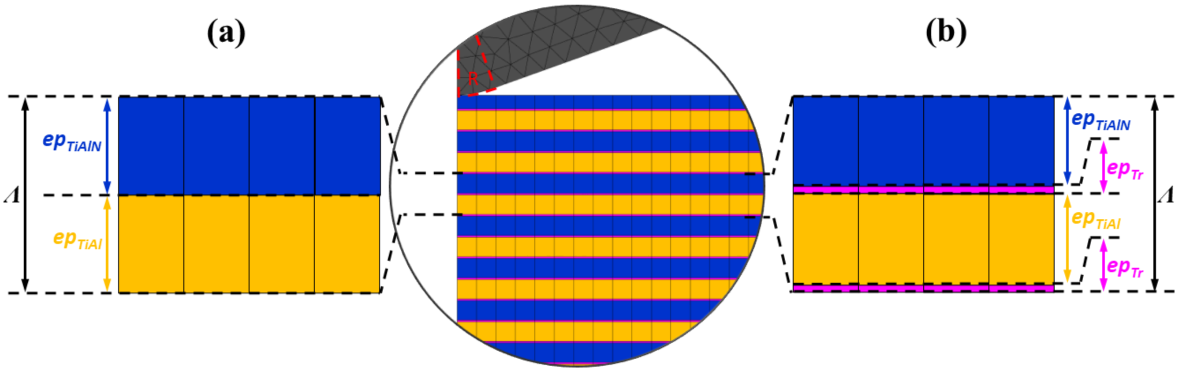

Fig. 1: An alternating stack of TiAl/TiAlN nanolayers with a) a perfect stacking, b) a transition layer.

The model is set for each stacking period Λ (Table 1).

A convergence study (data not shown) was carried out with 1, 2, 3 and 4 elements in the thickness of the layer and using 8 nodes quadrilateral elements (Q8) with quadratic interpolation (plane 183 element in ansys). Since the relative variation of the force is less than 0.1% and the von Mises contour are very similar with less than 0.5% difference on the maximum value, only one element (size $\Lambda/2$) in the thickness of the nanolayer was finally used, to minimise the calculation time.

2.4.2 Multilayer with a transition layer

The numerical model used for the multilayer coating with a transition layer is based on the FEM of the multilayer coating without transition layer. The coating is modelled as an assembly of TiAl and a TiAlN nanolayers stacked alternately with a transition layer of thickness ep_{Tr} between each TiAl and TiAlN layer (Fig. 1b) such as:

$$2e_{pTr} = \Lambda - (e_{pTiAl} + e_{pTiAlN}) \tag{11}$$

For the behaviour of the transition layer material, a mixture behaviour is assumed. Each material parameter p_{Tr} ($\equiv E_{Tr}, \nu_{Tr}, \sigma_{Y,Tr}, H_{p,Tr}$) of the transition layer is a mixture of the parameters of the two single TiAl and TiAlN parameter layer. To study the influence of the rule of mixtures on the indentation response, two possibilities, serial and parallel laws, are considered and defined respectively as follows:

$$\frac{1}{p_{Tr}} = \frac{1 - V_f}{p_{TiAl}} + \frac{V_f}{p_{TiAlN}} \tag{12}$$

$$p_{Tr} = (1 - V_f)p_{TiAl} + V_f p_{TiAlN} \tag{13}$$

The second possibility (parallel), sometimes used in the literature for the hardness of the multilayers, could be a signature of a columnar texture in the transition layer [55].

2.4.3 About the size/scale effect:

Finally, this finite element model reproduces the exact stacking of the coating. In this way, it is length scale dependant in the sense that the response of the material will depend on the indentation depths while no internal lengths is used directly in the definition of the different material's constitutive laws [56]. For multilayers, the value of the internal lengths is generally lower than the value of the period of the multilayer. The use of a such model would be justified if the behaviour of single interface was experimentally measured. However, this work focuses the mechanical behaviour of a single interface by the experimental measure of the mean response of multiple interfaces.

3 Results and Discussion

3.1 Monolithic TiAl and TiAlN coating properties

The crystallographic structure of TiAl and TiAlN monolithics are tetra or hexagonal and face-centred cubic respectively, as shown by the XRD patterns in ref [20]. Based on the experimental indentation curves (Fig. 2), the Young's modulus values of TiAl and TiAlN are 199 and 417 GPa respectively. The Poisson's ratio values were taken from the literature [22,57,58]: 0.25 and 0.21 for TiAl and TiAlN respectively.

The objective here was the robust identification of the two plastic parameters (σ_Y, H_p) of each TiAl and TiAlN monolithic coating sample from indentation curves obtained using the FEMU method and identifiability analysis. In a first step, some solutions (σ_Y, H_p) are obtained using the FEMU method from only the Berkovich P-h curve using the cost function (Eq. 6 with n=1). As shown in Fig. a, the numerical simulation at each solution point $\hat{\theta}$ (Eq. 5) are in good agreement with the experimental data.

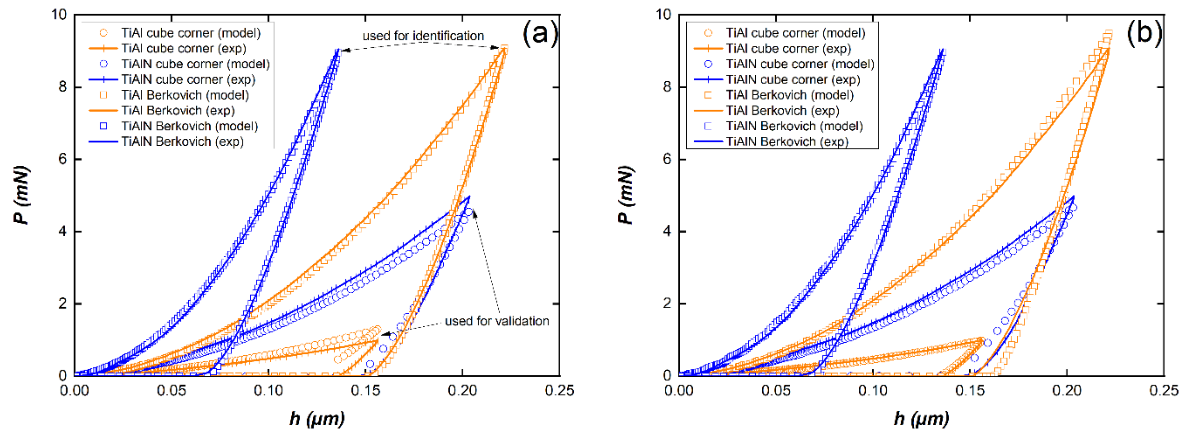

Fig. 2: Monolithic model-experiment comparison
(a) using one Berkovich P-h curve in the FEMU method and a cube corner for validation.
$(\sigma_Y, H_p) = (1.49\ GPa, 41.8\ GPa)$ *for TiAl and* $(14.6\ GPa, 25.2\ GPa)$ *for TiAlN,*

(b) using two P-h curves (Berkovich and cube corner) in the FEMU method.
$(\sigma_Y, H_p) = (3.44\ GPa, 6.33\ GPa)$ *for TiAl and* $(14.1\ GPa, 34.7\ GPa)$ *for TiAlN.*

The I-index values calculated from Equation 7 (7) are $I(TiAl) = 2.2$ and $I(TiAlN) = 3.7$. Unfortunately, for TiAlN, the I-index value is larger than 3, so too large to ensure the stability of the solution. The instability of the solution, i.e. the high sensitivity to experimental errors, indicates the existence of a valley of solutions of the functions $\omega(\sigma_Y, H_p)\sim 0$, classic in sharp indentation. Consequently, the model does not correctly predict cube corner tests (Fig. 2a).

In a second step, a priori identifiability analysis showed that adding a cube corner indentation curve reduces the I-index value (Eq. 7 with n=2). Using the FEMU method and the dual indentation technique, all the numerical simulations at each solution point $\hat{\theta}$ (Eq. 5) are in good agreement with the experimental data (Fig. b). Moreover, the I-index values calculated are $I(TiAl) = 2.1$ and $I(TiAlN) = 1.8$, so low enough (much lower than 3) to ensure acceptable stability of the solution.

Table 2 summarises the identified plastic properties of the monolithic coatings obtained using the FEMU method and the dual nanoindentation technique. It can be noted that the initial yield stress of TiAlN layers is about four times higher than that of TiAl.

Parameter		**TiAl**	**TiAlN**
$\hat{\theta}_1 = \sigma_Y$ (GPa)	initial yield stress	3.44	14.1
$\hat{\theta}_2 = H_p$ (GPa)	hardening modulus	6.33	34.7

Table 2: Plastic parameter values $\hat{\theta}_j$ of the monolithic coatings identified from Berkovich and cube corner P-h curves using the FEMU method

3.2 Multilayer coatings: effect of the stacking on the growth of the films and their nanoindentation response

The experimental Berkovich nanoindentation curves recorded for TiAl/TiAlN multilayer coatings (Fig. 3a) are located between those obtained for monolithic TiAl and TiAlN. These results are in good agreement with those obtained by Shugurov *et al.* [21] for TiAlN/TiAl multilayers with various periods.

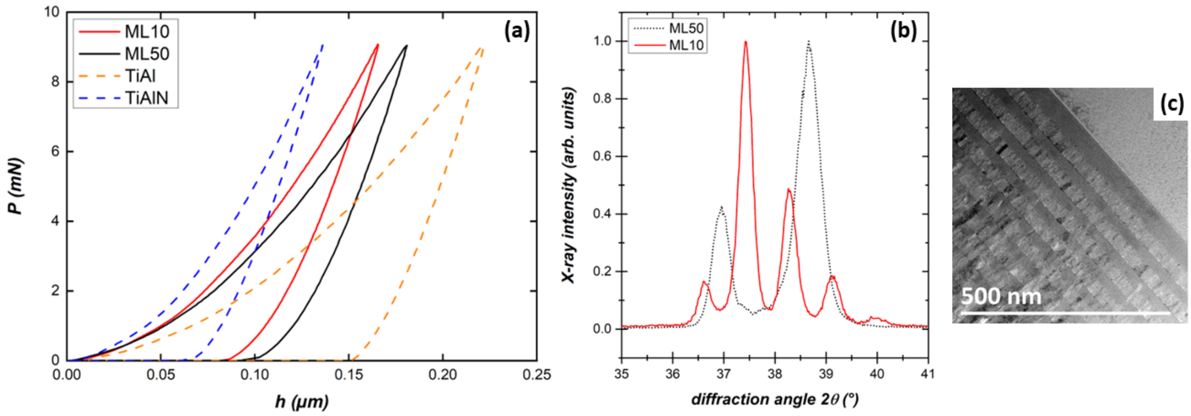

Fig. 3: (a) Experimental Berkovich nanoindentation curves on 10 and 50 nm period multilayer and monolithic coatings, (b) XRD patterns of the 10 and 50 nm period multilayer coatings and (c) bright filed STEM image of the cross-section of the 50 nm period multilayer coatings.

The XRD pattern (Fig. 3b) of the 10 nm period coating is characteristic of a well-defined superlattice with a main reflection flanked by satellite reflections. In contrast, for the 50 nm period film, whereas the multilayer stacking is clearly observable in the bright-field STEM image (Fig. 3c), the superstructure disappears and the satellite reflections are highly damped. Two dissociated peaks assigned to TiAlN ($2\theta = 36.9°$) and TiAl ($2\theta = 38.7°$) lattices are observed. Similar results are obtained from the SAED patterns of these two films. The intensity profile of the enlargement of the spot in the growth direction shows typical interferences of a superlattice and two distinct spots for the 10 and 50 nm period films respectively (Fig. 4a and 4b).

To demonstrate that the loss of the superlattice signature is related to the interface, a 50 nm period film was deposited with the same elaboration conditions using a shutter in front of the target during the deposition process between each nanolayer to obtain abrupt interfaces without a transition layer (ML50s). For this film, both the XRD pattern (Fig. 5b) and the intensity profile of the main spot in (Fig. 4c) show the two main reflections flanked by weak satellites, demonstrating the presence of nitrogen in the interface while the N_2

flow rate is cut off to deposit TiAl when the shutter is not applied. Consequently, a slightly higher experimental hardness (Fig. 5.a) is noticeable without the shutter (ML50) than with the shutter (ML50s) as the interfaces with transition layers containing nitrides are harder than metallic TiAl layers.

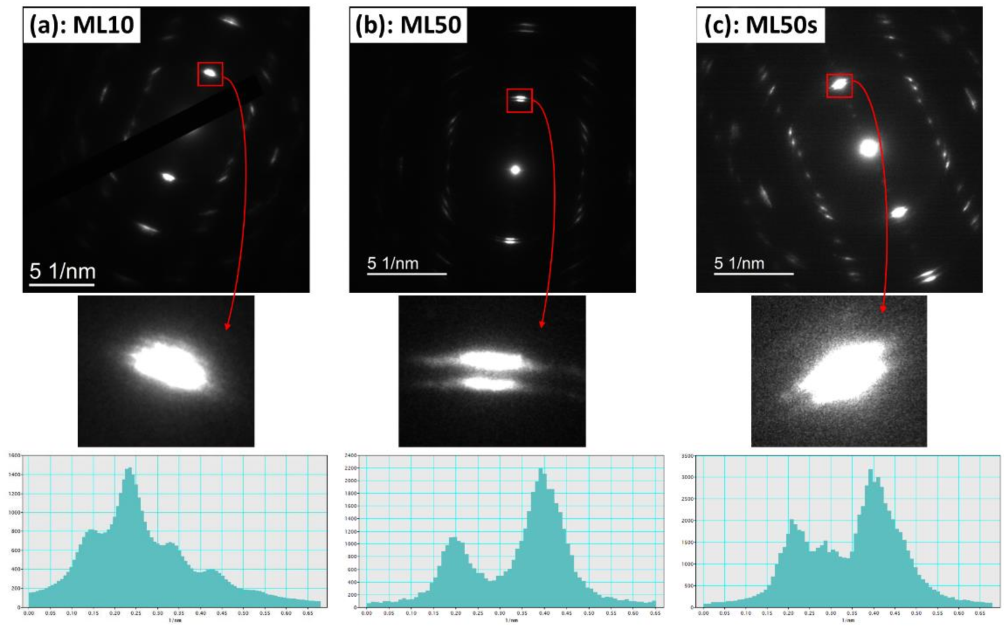

Fig. 4: SAED patterns of TiAl/TiAlN, enlargement of the spot along the growth direction and corresponding intensity profile for (a) 10 nm, (b) 50 nm and (c) 50 nm with shutter periods.

As a validation test of the behaviours of the two monolithic TiAl and TiAlN coatings identified using the FEMU method and the dual nanoindentation technique (Table 2), Berkovich and cube corner indentations were simulated on the 50 nm period multilayer coating sample with a shutter using the multilayer model without transition layer. As shown in Figure 5a, the predicted *P-h* curves are very close to the experimental ones. This result validates the properties of TiAl and TiAlN identified on monolithic coatings as the properties of the nanolayers in the multilayer stackings. It shows clearly also that it is possible to forecast the mechanical behaviour of a multilayer knowing the mechanical properties of its two constituents.

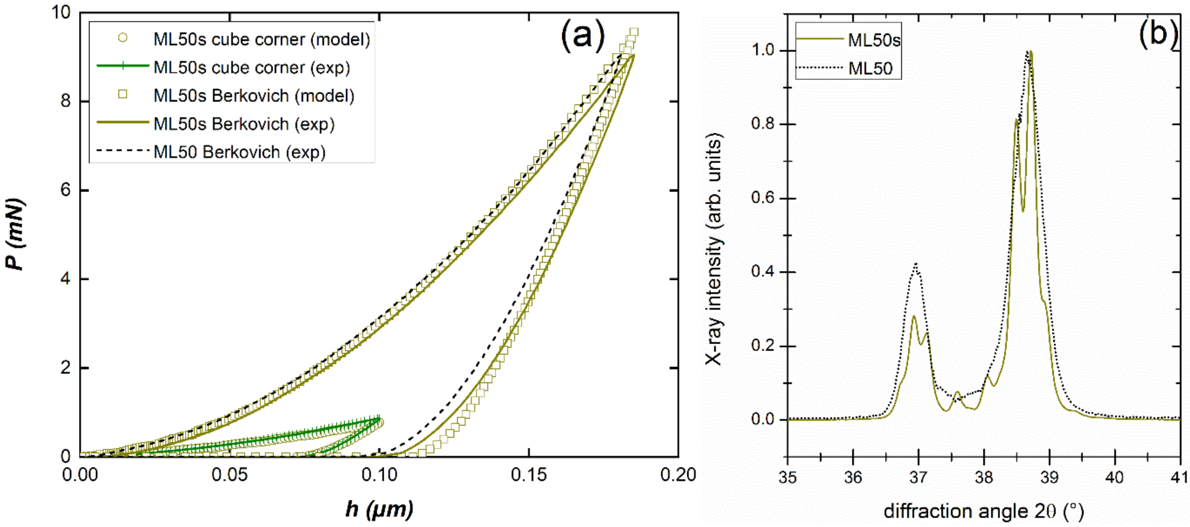

Fig. 5: (a) Experimental and model nanoindentation P-h curves and (b) XRD patterns of the 50 nm period multilayer coatings with a shutter (ML50s) and without a shutter (ML50)

3.3 Transition layer behaviour

3.3.1 Multilayers without transition layer

The numerical model used for the multilayer coating is based on the FEM of the monolithic coating behaviour identified in section **Erreur ! Source du renvoi introuvable.**. The coating is modelled as an assembly of alternately stacked layers of TiAl and TiAlN of equal thickness (5/5 and 25/25 nm for 10 and 50 nm period films respectively) (Fig. 1a). The TiAl/TiAlN interface is considered without thickness. The elastic-plastic behaviours of the TiAl and TiAlN layers identified in section 3.1 are introduced in the multilayer model. Figure 6 illustrates the *P-h* curves obtained using this model without transition layer. The predicted *P-h* curve is very close to the experimental one for the 50 nm-period film. However, for the low period one, the model does not forecast the increase in hardness observed experimentally.

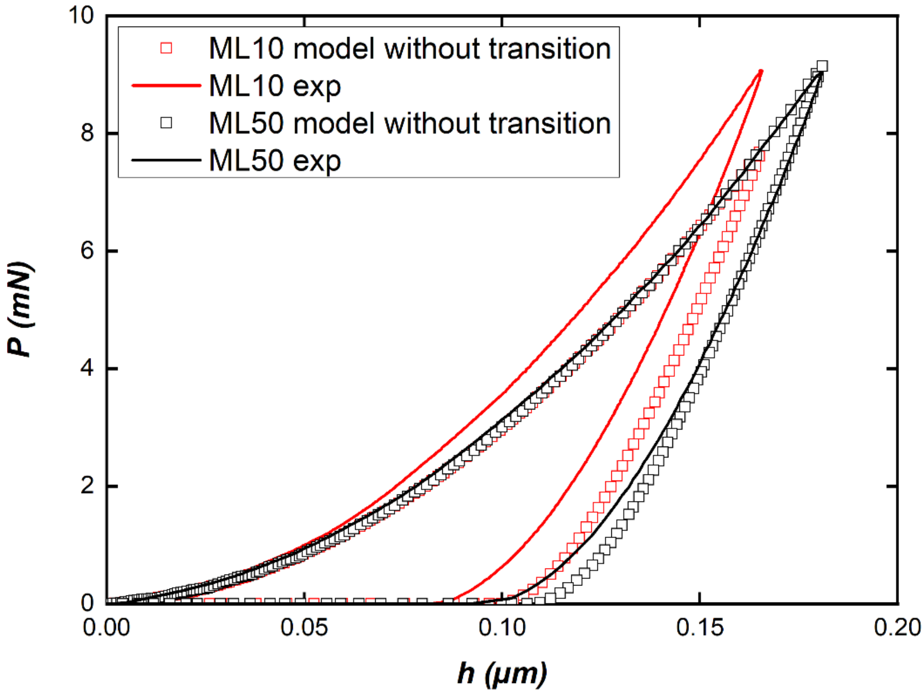

Fig. 6: Berkovich P-h curves for multilayer coating (periods 10 and 50 nm). Experiment-model comparison without transition layer ~~a perfect interface~~. Properties (E, σ_Y, H_p) of the monolithic layers: $(199\ GPa, 3.44\ GPa, 6.33\ GPa)$ for TiAl and $(417\ GPa, 14.1\ GPa, 34.7\ GPa)$ for TiAlN.

3.3.2 Multilayers with a transition layer

The numerical model used for the multilayer coating with a transition layer is based on the FEM of the multilayer coating without transition layer *i.e.* as an assembly of TiAl and TiAlN nanolayers with a transition layer of thickness ep_{Tr} (Eq. 11) between each TiAl and TiAlN layer (Fig. 1b). Each material parameter p_{Tr} of the transition layer ($p_{Tr} \equiv E_{Tr}, \nu_{Tr}, \sigma_{Y,Tr}, H_{p,Tr}$) is a mixture of the parameters of the TiAl and TiAlN monolithic layers. To study the influence of the rule of mixtures on the indentation response, two possibilities were considered: serial (Eq. 12) and parallel (Eq. 13). Considering the first results obtained by EELS, a 2 nm thickness transition layer is added, which represents a volume of about 8% and 40% of the total volume for the 50 nm and 10 nm period coatings respectively.

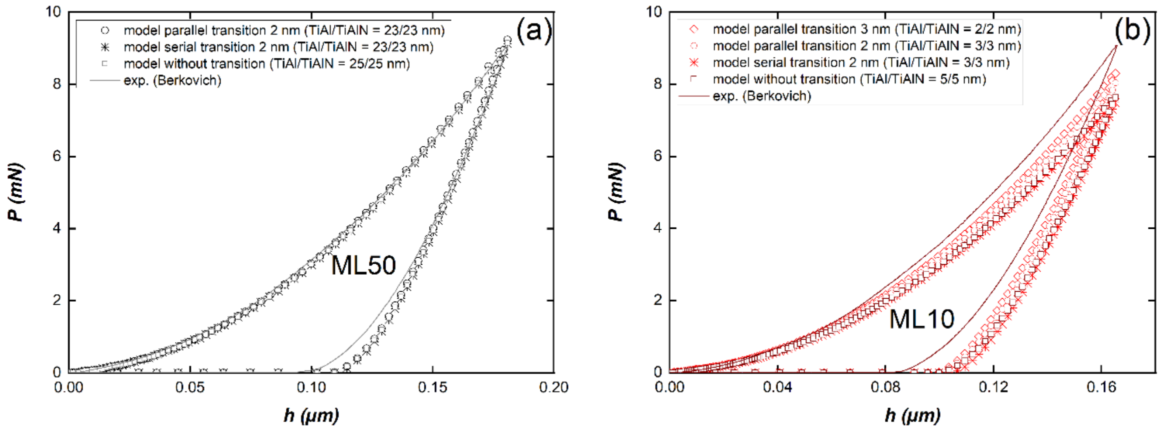

Fig. 7: Effect of a 2 nm-thickness transition layer on the simulated Berkovich P-h curves using the multilayers model. Model-experiment comparison with two mixture laws (serial and parallel) for the transition layer behaviour and two periods: (a) 50 nm and (b) 10 nm.
Properties (E, σ_Y, H_p) of the monolithic layers:
$(199{,}3.44{,}6.33)$ *GPa for TiAl and* $(417{,}14.1{,}34.7)$ *GPa for TiAlN.*

Figure 7 shows the simulated *P-h* curves, and a good agreement between model and experimental measurements is observed for the 50 nm period coating. For this film, the effect of the transition layer is very slight, whichever rule of mixtures is chosen. On the contrary, the model does not predict the loading force for the 10 nm-period multilayer. Even if the parallel rule of mixtures gives better results by providing a higher loading force, the predicted force is too low. Classically, interfaces impede the movement of dislocations and increase the strength of the material as described by Hall-Petch [56]. The addition of a nanometric interface with a particular material behaviour in the finite element model confers adequately this role to the interface boundaries. In fact, it is observed that plastic deformation is accumulated into ductile thin layer (Fig. 8).

A 3 nm transition layer was also tested (Fig. 7b) and demonstrated that differences between the experimental and model curves are not linked to the transition layer thickness, but probably to an imbalance between the thicknesses of the TiAl and TiAlN nanolayers.

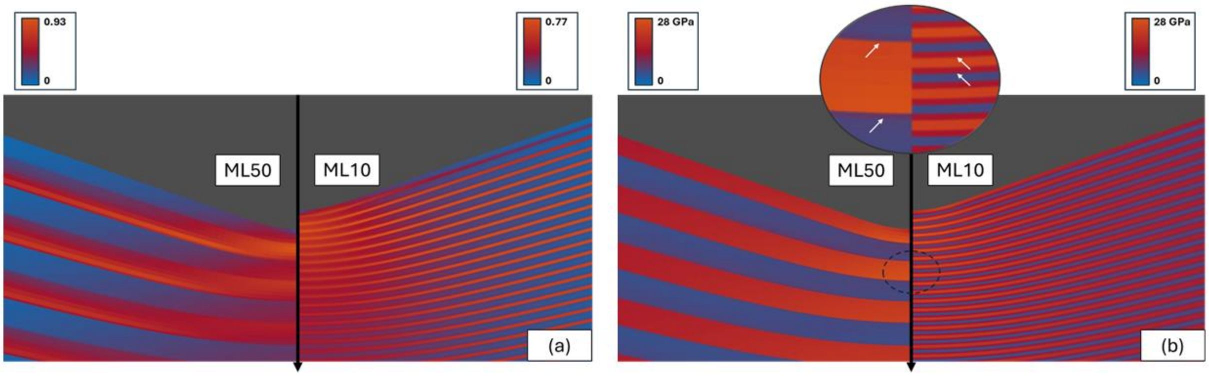

Fig. 8: Comparison between 50 nm and 10 nm period models showing the influence of the transition layer in the coating response during indentation: (a) plastic strain intensity and (b) equivalent von Mises stresses.

3.4 Imbalanced TiAl/TiAlN thickness

In previous sections equal thicknesses of TiAl and TiAlN layers were considered using a TiAlN volume fraction parameter V_f (eq. 10) equal to 0.5. To increase predicted force in the model, V_f should be greater than 0.5 to raise nitride volume fraction in the coating. In order to determine this value and quantify the thickness imbalance between the metal TiAl and nitride TiAlN layers, quantitative EELS profiles were used.

3.4.1 Thicknesses of the nanolayers in the stacking by EELS

N K-edge electron energy loss spectroscopy was used to characterise the element composition of the interfaces between the TiAl/TiAlN and TiAlN/TiAl transitions. From the EELS spectra, the relative concentration of the nitrogen and titanium elements were recorded every 0.3 nm and plotted in Figure 9. For both periods, the transition zone from the TiAl to TiAlN nanolayers and from the TiAlN to TiAl ones has the same thickness of about 2-3 nm. However, the multilayer architecture is imbalanced: the thickness of the TiAlN nanolayers is greater than that of the TiAl nanolayers. For the 10 nm period sample, the thickness of the nitride layers measures 3.80 ± 0.20 nm while the TiAl metal layers measure 1.50 ± 0.50 nm and the transition layer shows a 2.35 ± 0.40 nm-thickness. The

50 nm period sample exhibits a thickness of TiAlN and TiAl layers of 27 ± 1 nm and 21 ± 1 nm with a 3 ± 0.3 nm transition thickness nanolayers (the thickness values are averaged from 5 measurements). These results clearly show the presence of a nitrogen concentration gradient in the transition layers due to the closing and opening of the nitrogen flow during the deposition process. But the effect is not the same for both coatings since this gradient represents a very high volume fraction for the low period sample: 48% compared to 12% for the high period sample. This precise knowledge of the cross-sectional microstructure of the stacking has been added to the models.

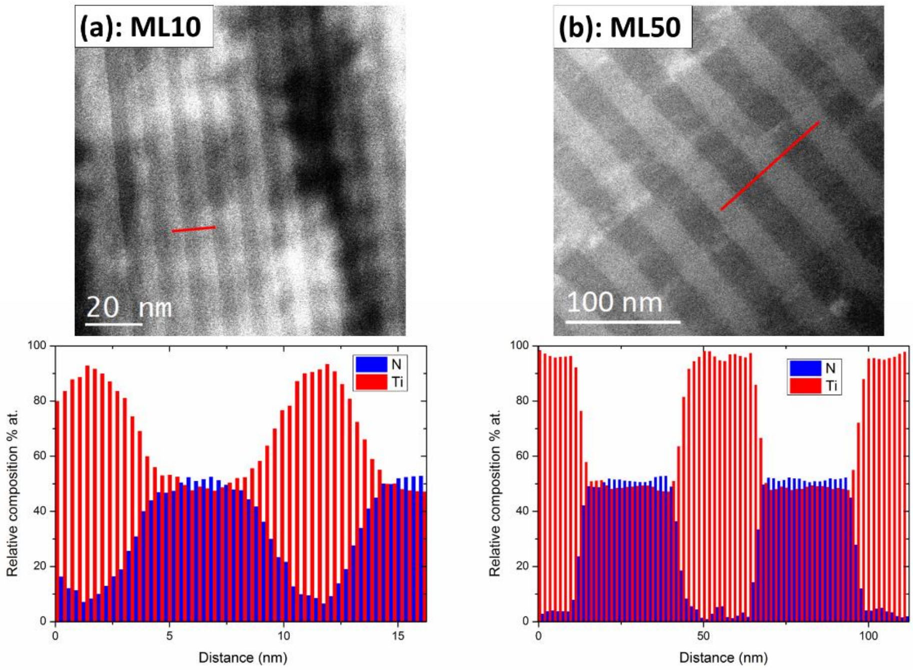

Fig. 9: Dark-field STEM image of the cross-section of TiAl/TiAlN multilayered film a) Λ = 10 nm, b) Λ = 50 nm and corresponding relative concentration of N and Ti elements recorded along the a) 16 nm and b)112 nm red line.

3.4.2 Effect of TiAlN/TiAl thickness ratio on simulated P-h curves

Based on microstructural determination, the solutions TiAl/TiAlN=1.5 nm/3.8 nm with a 2.35 nm transition layer thickness for the 10 nm period film and TiAl/TiAlN = 21 nm/27 nm with a 3 nm transition layer thickness for the 50 nm period coating are used in the models. As shown in Fig. a and 10b, the simulated *P-h* curves are very close to the experimental ones for both periods, whatever the rule of mixtures chosen for the transition layer. For the higher period specimen, the hypothesis on the rule of mixtures has a negligible influence on the result while for the low period specimen, the loading force is slightly overestimated with the parallel hypothesis and slightly underestimated with the serial hypothesis.

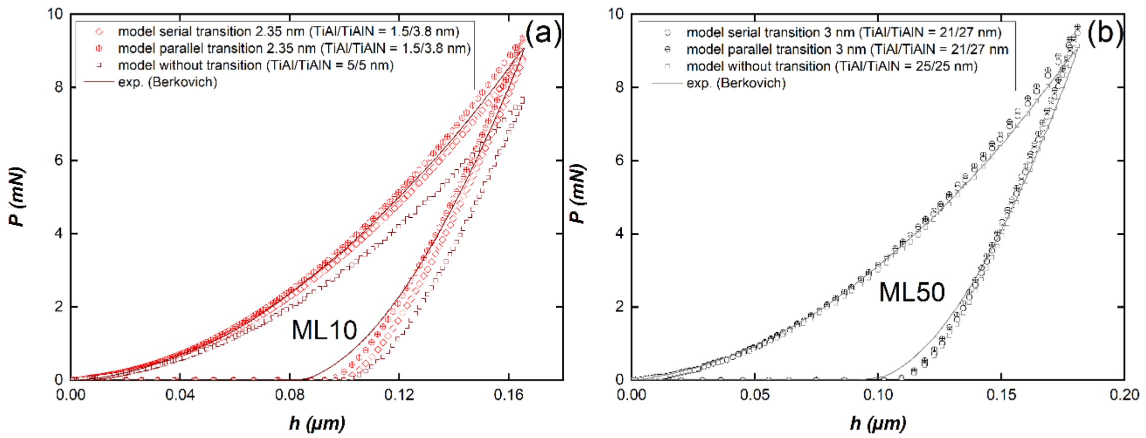

Fig. 10: Effect of imbalanced TiAlN/TiAl thickness and rule of mixtures on simulated Berkovich P-h curve a)10 nm and (b) 50 nm period. Properties (E, σ_Y, H_p)*:* $(199, 3.44, 6.33)$ *GPa for TiAl and* $(417, 14.1, 34.7)$ *GPa for TiAlN.*

As the contact area can also be evaluated numerically, it is possible to compare numerical and experimental hardness. Figure 11a shows the hardness obtained experimentally and numerically for the monolayer and the multilayer films considering the two rules of mixture evocated previously in the case of the 10 nm period film and only the serial hypothesis in the case of the 50 nm period film. It can be observed that the material properties found from the inverse analysis can be used to predict the hardness of the different coatings. From this figure, the serial hypothesis clearly matches better with the experiments than the parallel one. Indentation reduced modulus can also be calculated numerically as a function of depth, applying a particular sinusoidal loading [59]. Figure 11b shows the comparison between numerical and experimental reduced indentation modulus obtained from continuous stiffness measurements. Due to limit conditions, it is well known that elastic properties are less well extracted by finite element modelling than plastic ones, however, if numerical and experimental values of modulus do not match as well as the ones of hardnesses, the gap between experimental and numerical values remains under 10%, 3% for TiAlN, 8% for the 10nm multilayer, 9% for TiAl and 10% for the 50nm multilayer. Particularly, the gap between the 10 and the 50nm multilayer is well reproduced by the model. Indeed, the models used turns out to be very predictive as in reality the microstructure of the transition layer is complex and probably similar to a nitride concentration gradient in the transition layer thickness.

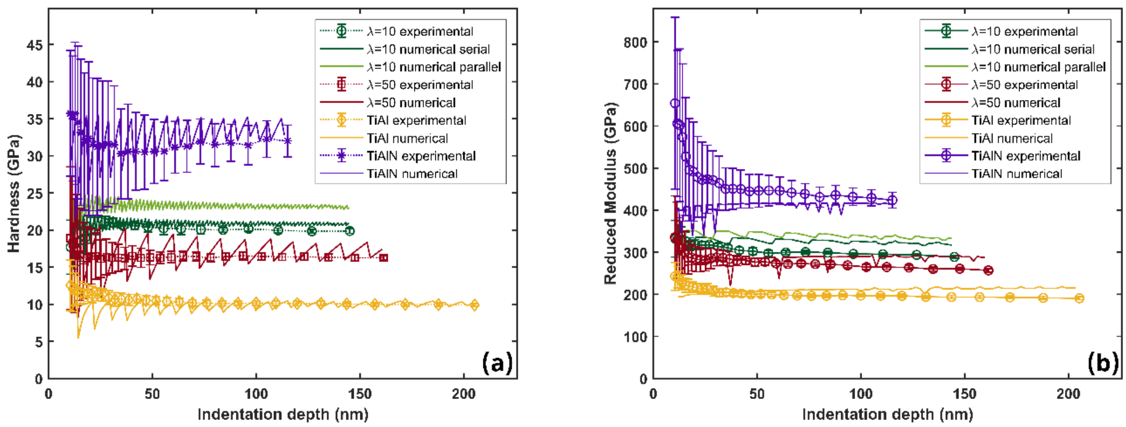

Fig. 11: Comparison between numerical (with serial and parallel hypotheses for the 10 nm period and serial hypothesis for the 50 nm period) and experimental data obtained for multilayer and monolayer coatings: (a) hardness and (b) indentation reduced modulus

4 Conclusions

In this paper, thin $Ti_{0.67}Al_{0.33}/Ti_{0.54}Al_{0.46}N$ (named TiAl/TiAlN) multilayer coatings were deposited by radio-frequency magnetron sputtering from a single sintered titanium/aluminium target using the reactive gas pulsing process. A finite element model reproducing the mechanical behaviour of those stacked nanolayer coatings during an indentation test was developed and used to identify reliably, using an identifiability index, plastic properties following a FEMU process. The following conclusions can be drawn:

1. the mechanical behaviour of a 50 nm period multilayer, deposited with a shutter in front of the target between each stack, can be predicted from the mechanical behaviour of its two main constituents, themselves reliably identified from a dual indentations FEMU process.

2. without a shutter and for shorter periods, the introduction of a specific interlayer is necessary to reproduced faithfully the mechanical behaviour of the multilayers. This interlayer (transition layer) is observed, measured, and characterised experimentally by TEM and N_2 concentration determination by quantification of EELS profile spectra containing N K-edge and Ti L-edge. It is a nanometric layer with a gradient of nitrogen.

3. based on the true architecture of the multilayers, it is found that the mechanical properties of this interlayer can be well described by a mixture law and a serial hypothesis. This is established by comparing numerical and experimental indentation behaviour of a 10 nm and 50 nm multilayer coatings.

4. taking into account the true structure of the multilayer appears to be sufficient to reproduce the indentation response of such materials. Compared to classical analytical models accounting for hardness [56], not only the hardnesses but also the indentation moduli appear to be well predicted and evaluated in this work.

Finally, as the transition layer contain a strong gradient in nitrogen, its mechanical description deserves to be refined. In this aim, atomistic studies should be conducted specifically in this domain. The size of the considered region appears to be particularly suitable. It would certainly further improve the match between numerical and experimental response.

Acknowledgements

The authors acknowledge the support of the French Agence Nationale de la Recherche (ANR), under grant ANR-10-AIRT-04 (project RESEM 2019/NANOSTRAT) and ANR-22-CE08-0008 (project MULTI-NANO-ULHC). The authors also thank the local authority “Pays Montbeliard Agglomération” for its financial support (Contract 20161016061). The authors also wish to acknowledge D. Troadec at IEMN, Lille, for the FIB lamella production.

References

[1] S. PalDey, S.C. Deevi, Single layer and multilayer wear resistant coatings of (Ti,Al)N: a review, Mater. Sci. Eng. A 342 (2003) 58–79. https://doi.org/10.1016/S0921-5093(02)00259-9.
[2] T. Vieira, J. Castanho, C. Louro, Chapter 16 - Hard Coatings Based on Metal Nitrides, Metal Carbides and Nanocomposite Materials: PVD Process and Properties, in: Y. Pauleau (Ed.), Mater. Surf. Process. Dir. Energy Tech., Elsevier, Oxford, 2006: pp. 537–572. https://doi.org/10.1016/B978-008044496-3/50017-4.
[3] F. Uny, E. Blanquet, F. Schuster, F. Sanchette, Ti-Al-N-Based Hard Coatings: Thermodynamical Background, CVD Deposition, and Properties. A Review, in: J. Andres Perez-Taborda, A. G. Avila Bernal (Eds.), Coat. Thin-Film Technol., IntechOpen, 2019. https://doi.org/10.5772/intechopen.79747.
[4] S. Zhang, D. Sun, Y. Fu, Y.T. Pei, J.Th.M. De Hosson, Ni-toughened nc-TiN/a-SiNx nanocomposite thin films, Surf. Coat. Technol. 200 (2005) 1530–1534. https://doi.org/10.1016/j.surfcoat.2005.08.080.
[5] C. Wang, K. Shi, C. Gross, J.M. Pureza, M. de Mesquita Lacerda, Y.-W. Chung, Toughness enhancement of nanostructured hard coatings: Design strategies and toughness measurement techniques, Surf. Coat. Technol. 257 (2014) 206–212. https://doi.org/10.1016/j.surfcoat.2014.08.018.
[6] J.M. Molina-aldareguia, S.J. Lloyd, M. Odén, T. Joelsson, L. Hultman, W.J. Clegg, Deformation structures under indentations in TiN/NbN single-crystal multilayers deposited by magnetron sputtering at different bombarding ion energies, Philos. Mag. A 82 (2002) 1983–1992. https://doi.org/10.1080/01418610208235710.
[7] E. Martínez, J. Romero, A. Lousa, J. Esteve, Nanoindentation stress–strain curves as a method for thin-film complete mechanical characterization: application to nanometric CrN/Cr multilayer coatings, Appl. Phys. A 77 (2003) 419–426. https://doi.org/10.1007/s00339-002-1669-0.
[8] N.J.M. Carvalho, J.Th.M. De Hosson, Deformation mechanisms in TiN/(Ti,Al)N multilayers under depth-sensing indentation, Acta Mater. 54 (2006) 1857–1862. https://doi.org/10.1016/j.actamat.2005.12.010.
[9] J. Shi, Z.H. Cao, Y. Liu, Z.P. Zhao, Size dependent alloying and plastic deformation behaviors of Ti/Ni nano-multilayers, J. Alloys Compd. 727 (2017) 691–695. https://doi.org/10.1016/j.jallcom.2017.08.158.
[10] Z.H. Xie, M. Hoffman, P. Munroe, A. Bendavid, P.J. Martin, Deformation mechanisms of TiN multilayer coatings alternated by ductile or stiff interlayers, Acta Mater. 56 (2008) 852–861. https://doi.org/10.1016/j.actamat.2007.10.047.

[11] T. Fu, X. Peng, S. Weng, Y. Zhao, F. Gao, L. Deng, Z. Wang, Molecular dynamics simulation of effects of twin interfaces on Cu/Ni multilayers, Mater. Sci. Eng. A 658 (2016) 1–7. https://doi.org/10.1016/j.msea.2016.01.055.
[12] T.E.J. Edwards, T. Xie, N. Maria della Ventura, D. Casari, C. Guerra, E. Huszár, X. Maeder, J.J. Schwiedrzik, I. Utke, L. Pethö, J. Michler, On the thinnest Al2O3 interlayers in Al-based nanolaminates to enhance strength, and the role of constraint, Acta Mater. 240 (2022) 118345. https://doi.org/10.1016/j.actamat.2022.118345.
[13] Z. Chen, Y. Zheng, Y. Huang, Z. Gao, H. Sheng, M. Bartosik, P.H. Mayrhofer, Z. Zhang, Atomic-scale understanding of the structural evolution of TiN/AlN superlattice during nanoindentation— Part 1: Deformation, Acta Mater. 234 (2022) 118008. https://doi.org/10.1016/j.actamat.2022.118008.
[14] Z. Chen, Y. Zheng, Y. Huang, Z. Gao, H. Sheng, M. Bartosik, P.H. Mayrhofer, Z. Zhang, Atomic-scale understanding of the structural evolution in TiN/AlN superlattice during nanoindentation—Part 2: Strengthening, Acta Mater. 234 (2022) 118009. https://doi.org/10.1016/j.actamat.2022.118009.
[15] R. Bermejo, Y. Torres, A. Sanchezherencia, C. Baudin, M. Anglada, L. Llanes, Residual stresses, strength and toughness of laminates with different layer thickness ratios, Acta Mater. 54 (2006) 4745–4757. https://doi.org/10.1016/j.actamat.2006.06.008.
[16] A.K. Mishra, H. Gopalan, M. Hans, C. Kirchlechner, J.M. Schneider, G. Dehm, B.N. Jaya, Strategies for damage tolerance enhancement in metal/ceramic thin films: Lessons learned from Ti/TiN, Acta Mater. 228 (2022) 117777. https://doi.org/10.1016/j.actamat.2022.117777.
[17] G. Tang, Y.-L. Shen, D.R.P. Singh, N. Chawla, Indentation behavior of metal–ceramic multilayers at the nanoscale: Numerical analysis and experimental verification, Acta Mater. 58 (2010) 2033–2044. https://doi.org/10.1016/j.actamat.2009.11.046.
[18] X.H. Tan, Y.-L. Shen, Modeling analysis of the indentation-derived yield properties of metallic multilayered composites, Compos. Sci. Technol. 65 (2005) 1639–1646. https://doi.org/10.1016/j.compscitech.2004.12.051.
[19] M.-J. Pac, S. Giljean, C. Rousselot, F. Richard, P. Delobelle, Microstructural and elasto-plastic material parameters identification by inverse finite elements method of Ti (1−x) Al x N (0 < x < 1) sputtered thin films from Berkovich nano-indentation experiments, Thin Solid Films 569 (2014) 81–92. https://doi.org/10.1016/j.tsf.2014.07.037.
[20] M.-J. Pac, Y. Pinot, S. Giljean, C. Rousselot, P. Delobelle, C. Ulhaq-Bouillet, M.-H. Tuilier, Investigation of Ti 0.54 Al 0.46 /Ti 0.54 Al 0.46 N multilayer films deposited by reactive gas pulsing process by nano-indentation and electron energy-loss spectroscopy, Thin Solid Films 634 (2017) 96–106. https://doi.org/10.1016/j.tsf.2017.05.015.
[21] A.R. Shugurov, M.S. Kazachenok, Mechanical properties and tribological behavior of magnetron sputtered TiAlN/TiAl multilayer coatings, Surf. Coat. Technol. 353 (2018) 254–262. https://doi.org/10.1016/j.surfcoat.2018.09.001.
[22] L. Chen, J. Xu, M. Zhang, T. Rong, Z. Jiang, P. Li, Systematic study on mechanical and electronic properties of ternary VAlN, TiAlN and WAlN systems by first-principles calculations, Ceram. Int. 47 (2021) 7511–7520. https://doi.org/10.1016/j.ceramint.2020.11.090.
[23] S. Liu, K. Chang, D. Music, X. Chen, S. Mráz, D. Bogdanovski, M. Hans, D. Primetzhofer, J.M. Schneider, Stress-dependent prediction of metastable phase formation for magnetron-sputtered V1−xAlxN and Ti1−xAlxN thin films, Acta Mater. 196 (2020) 313–324. https://doi.org/10.1016/j.actamat.2020.06.044.
[24] S. Liu, K. Chang, S. Mráz, X. Chen, M. Hans, D. Music, D. Primetzhofer, J.M. Schneider, Modeling of metastable phase formation for sputtered Ti1-xAlxN thin films, Acta Mater. 165 (2019) 615–625. https://doi.org/10.1016/j.actamat.2018.12.004.
[25] F. Tasnadi, I.A. Abrikosov, L. Rogström, J. Almer, M.P. Johansson, M. Oden, Significant elastic anisotropy in Ti$_{1-x}$Al$_x$N alloys, Appl. Phys. Lett. 97 (2010) 231902. https://doi.org/10.1063/1.3524502.
[26] K. Kutschej, P.H. Mayrhofer, M. Kathrein, P. Polcik, R. Tessadri, C. Mitterer, Structure, mechanical and tribological properties of sputtered Ti1−xAlxN coatings with

0.5≤x≤0.75, Surf. Coat. Technol. 200 (2005) 2358–2365. https://doi.org/10.1016/j.surfcoat.2004.12.008.
[27] M.-H. Tuilier, M.-J. Pac, G. Covarel, C. Rousselot, L. Khouchaf, Structural investigation of thin films of Ti1−xAlxN ternary nitrides using Ti K-edge X-ray absorption fine structure, Surf. Coat. Technol. 201 (2007) 4536–4541. https://doi.org/10.1016/j.surfcoat.2006.09.095.
[28] Y.-T. Cheng, C.-M. Cheng, Can stress–strain relationships be obtained from indentation curves using conical and pyramidal indenters?, J. Mater. Res. 14 (1999) 3493–3496.
[29] F. Richard, M. Villars, S. Thibaud, Viscoelastic modeling and quantitative experimental characterization of normal and osteoarthritic human articular cartilage using indentation, J. Mech. Behav. Biomed. Mater. 24 (2013) 41–52. https://doi.org/10.1016/j.jmbbm.2013.04.012.
[30] V. Fauvel, Y. Gaillard, R. Guillemet, P. Garabédian, F. Richard, Simultaneous extraction of the elastic-plastic properties of a thin film and its substrate from an identifiability-based design of depth-sensing nanoindentation testing, J. Mech. Phys. Solids (2022) 104860. https://doi.org/10.1016/j.jmps.2022.104860.
[31] P. Wieciński, J. Smolik, H. Garbacz, K.J. Kurzydłowski, Failure and deformation mechanisms during indentation in nanostructured Cr/CrN multilayer coatings, Surf. Coat. Technol. 240 (2014) 23–31. https://doi.org/10.1016/j.surfcoat.2013.12.006.
[32] R. Hahn, M. Bartosik, R. Soler, C. Kirchlechner, G. Dehm, P.H. Mayrhofer, Superlattice effect for enhanced fracture toughness of hard coatings, Scr. Mater. 124 (2016) 67–70. https://doi.org/10.1016/j.scriptamat.2016.06.030.
[33] M. Shinn, S.A. Barnett, Effect of superlattice layer elastic moduli on hardness, Appl. Phys. Lett. 64 (1994) 61–63. https://doi.org/10.1063/1.110922.
[34] B. Schmid, N. Koutná, E. Ntemou, D. Primetzhofer, T. Wojcik, S. Kolozsvari, P.H. Mayrhofer, Mechanical Properties of VC/ZrC and VC/HfC Superlattices, Acta Mater. (2024) 119852. https://doi.org/10.1016/j.actamat.2024.119852.
[35] C. Gu, F. Wang, P. Huang, K.W. Xu, T.J. Lu, Structure-dependent size effects in CuTa/Cu nanolaminates, Mater. Sci. Eng. A 658 (2016) 381–388. https://doi.org/10.1016/j.msea.2016.01.118.
[36] H. Zhou, L. Chang, K. Fu, H. Huang, R. Niu, X. Liao, L. Sheppard, L. George, L. Martinu, Improvement of flow strength and scratch resistance of Ti/Cu nanocrystalline metal multilayer thin films by tailoring layer thickness and modulation ratio, Surf. Coat. Technol. 404 (2020) 126461. https://doi.org/10.1016/j.surfcoat.2020.126461.
[37] Y. Pinot, M.-J. Pac, P. Henry, C. Rousselot, Ya.I. Odarchenko, D.A. Ivanov, C. Ulhaq-Bouillet, O. Ersen, M.-H. Tuilier, Friction behaviour of TiAlN films around cubic/hexagonal transition: A 2D grazing incidence X-ray diffraction and electron energy loss spectroscopy study, Thin Solid Films 577 (2015) 74–81. https://doi.org/10.1016/j.tsf.2015.01.044.
[38] Martin N. et al., Procédé de pulvérisation réactive à signal de commande cyclique et dispositif correspondant, Patent Fr 2905124 (2008). Patent Fr 2905124.
[39] W.C. Oliver, G.M. Pharr, An improved technique for determining hardness and elastic modulus using load and displacement sensing indentation experiments, J. Mater. Res. 7 (1992) 1564–1583. https://doi.org/10.1557/JMR.1992.1564.
[40] W.C. Oliver, G.M. Pharr, Measurement of hardness and elastic modulus by instrumented indentation: Advances in understanding and refinements to methodology, J. Mater. Res. 19 (2004) 3–20. https://doi.org/10.1557/jmr.2004.19.1.3.
[41] J.L. Bucaille, S. Stauss, E. Felder, J. Michler, Determination of plastic properties of metals by instrumented indentation using different sharp indenters, Acta Mater. 51 (2003) 1663–1678. https://doi.org/10.1016/S1359-6454(02)00568-2.
[42] K. Levenberg, A method for the solution of certain non-linear problems in least squares, Q. Appl. Math. 2 (1944) 164–168.
[43] D.W. Marquardt, An algorithm for least-squares estimation of nonlinear parameters, J. Soc. Ind. Appl. Math. 11 (1963) 431–441.

[44] F. Richard, MIC2M Software: Modélisation et Identification du Comportement Mécanique des Matériaux/Modeling and Identification of the Mechanical Behavior of Materials, 2000. http://mic2m.univ-fcomte.fr.
[45] M. Qasmi, P. Delobelle, F. Richard, C. Brun, M. Fromm, Viscoelastic mechanical properties determined by nanoindentation tests and its numerical modelling of polypropylene modified by He+ particle implantation and e- irradiation, Prog. Org. Coat. 51 (2004) 195–204.
[46] T.W. Capehart, Y.T. Cheng, Determining constitutive models from conical indentation: Sensitivity analysis, J. Mater. Res. 18 (2003) 827–832.
[47] J. Alkorta, J.M. Martinez-Esnaola, J.G. Sevillano, Absence of one-to-one correspondence between elastoplastic properties and sharp-indentation load–penetration data, J. Mater. Res. 20 (2005) 432–437.
[48] M.-Q. Le, A computational study on the instrumented sharp indentations with dual indenters, Int. J. Solids Struct. 45 (2008) 2818–2835.
[49] C. Heinrich, A.M. Waas, A.S. Wineman, Determination of material properties using nanoindentation and multiple indenter tips, Int. J. Solids Struct. 46 (2009) 364–376.
[50] M.-Q. Le, Improved reverse analysis for material characterization with dual sharp indenters, Int. J. Solids Struct. 48 (2011) 1600–1609.
[51] X. Chen, N. Ogasawara, M. Zhao, N. Chiba, On the uniqueness of measuring elastoplastic properties from indentation: the indistinguishable mystical materials, J. Mech. Phys. Solids 55 (2007) 1618–1660.
[52] J.K. Phadikar, T.A. Bogetti, A.M. Karlsson, On the uniqueness and sensitivity of indentation testing of isotropic materials, Int. J. Solids Struct. 50 (2013) 3242–3253. https://doi.org/10.1016/j.ijsolstr.2013.05.028.
[53] F. Anstett-Collin, L. Denis-Vidal, G. Millérioux, A priori identifiability: An overview on definitions and approaches, Annu. Rev. Control 50 (2020) 139–149. https://doi.org/10.1016/j.arcontrol.2020.10.006.
[54] E. Walter, L. Pronzato, Identification of parametric models from experimental data, Springer ; Masson, Berlin; New York; Paris, 1997.
[55] M.D. Gram, J.S. Carpenter, P.M. Anderson, An indentation-based method to determine constituent strengths within nanolayered composites, Acta Mater. 92 (2015) 255–264. https://doi.org/10.1016/j.actamat.2015.04.002.
[56] A. Misra, J.P. Hirth, R.G. Hoagland, Length-scale-dependent deformation mechanisms in incoherent metallic multilayered composites, Acta Mater. 53 (2005) 4817–4824. https://doi.org/10.1016/j.actamat.2005.06.025.
[57] Y. He, R.B. Schwarz, A. Migliori, S.H. Whang, Elastic constants of single crystal y - TiAl, J Mater Res 10 (1995).
[58] Y. Wen, L. Wang, H. Liu, L. Song, Ab Initio Study of the Elastic and Mechanical Properties of B19 TiAl, Crystals 7 (2017) 39. https://doi.org/10.3390/cryst7020039.
[59] Y. Gaillard, E. Jimenez-Piqué, M. Oliva-Ramirez, V.J. Rico, A.R. Gonzalez-Elipe, Extraction of microstructural parameters from sculptured thin films nanoindentation, Surf. Coat. Technol. 425 (2021) 127696. https://doi.org/10.1016/j.surfcoat.2021.127696.